Determination of Microsphere-Lens Magnification Using Micro-Robotic Scanning Superlens Nanoscopy

BOLIANG JIA [1], **PAN LI**[2], **FEIFEI WANG**[3], **HO YIN CHAN**[1], **GUANGLIE ZHANG**[1], **AND WEN JUNG LI** [1]

[1] Department of Mechanical Engineering, City University of Hong Kong, Hong Kong 999077, China
[2] College of Mechanical and Electrical Engineering, Hohai University, Jiangsu 213022, China
[3] Department of Chemistry, Stanford University, Stanford, CA 94305 USA
[4] Shenzhen Academy of Robotics, Shenzhen 518000, China

CORRESPONDING AUTHORS: GUANGLIE ZHANG; WEN JUNG LI (e-mail: gl.zhang@cityu.edu.hk; wenjli@cityu.edu.hk)

ABSTRACT Microsphere-assisted nanoscopy has shown great potential in recent developments in the field of super-resolution imaging. The precise control of microspheres is leading to new discoveries that can help verify the theories behind the super-resolution imaging mechanism. However, microsphere imaging involves multiple planes that have different magnification factors, which affect the determination of the overall resolution of the image. In this study, we present a flexible probe–lens assembly scheme that uses a barium titanate glass microsphere, as well as various scanning stages that can be used to freely investigate the sample surface and perform large-area super-resolution imaging (80 μm × 60 μm). The obtained resolution using this assembly under water immersion condition is 130 nm. By investigating the relationship between the magnification factors and the corresponding focus position of the different feature patterns, a remarkable difference in the focusing characteristics between arbitrary and periodic patterns was revealed. Results demonstrate the universality of the proposed method for the quantitative selection of the best focused plane and determination of the corresponding magnification factor and resolution of a microsphere virtual image for any feature pattern. The findings provide additional insights into the interpretation of arbitrary nanostructures through 3D optical imaging.

INDEX TERMS Super-resolution imaging, dielectric microsphere, scanning superlens microscopy, scanning probe–lens microscopy, magnification factor, micro-robotics.

I. INTRODUCTION

Optical microscopy played an irreplaceable role in the modern science and technology. Several of its properties, such as real-time processing, non-destructiveness, and versatile imaging, are essential requirements for a wide range of applications, including life science, chemistry, and material science. With the development of super-resolution microscopy, the diffraction limit [1], [2] of half of the visible wavelength has been overcome after more than 100 years since its discovery. The existing super-resolution technologies can be categorized into far- or near-field optics. Far-field super-resolution imaging approach aims to reduce the size of the point spread function (PSF) of the optical system by using specialized illumination configurations, fluorescent dyes as detection molecule,

and several computing algorithms to reconstruct the image, such as stimulated emission depletion (STED) microscopy [3] and stochastic optical reconstruction microscopy (STORM) [4]. Conversely, near-field techniques do not rely on special illuminations or fluorescent labels, but rather use near-field probes to collect high-spatial frequency information within the proximity of the sample before reconstructing the image. For example, scanning near-field microscopy (SNOM) [5] utilizes a sharply tapered probe to scan a sample's surface at a distance of a few tens of nanometers [6]. SNOM-related technology benefits from the advancement of high-precision manipulation stages in scanning tunneling microscopy [7]. In the recent years, a new type of near-field acquisition lens called microsphere superlens has attracted substantial

attention due to its simple implementation and integration, high-adaptability to conventional optical systems, and superior imaging resolution.

Microsphere-assisted nanoscopy was developed after discovering its capability to generate subdiffraction-limited nanopatterns in the field of laser cleaning [8]. In 2011, Wang et al. experimentally demonstrated the use of silica microspheres with diameter (D) of 2–9 μm, which were placed on the top of sample surfaces, to resolve the subdiffraction-limited structures using an ordinary optical microscope [9]. Their work started the research on optical nano-imaging through microspheres. Given the excellent compatibility of this approach with the existing microscopy platforms and its adaptability to different kinds of samples, the applications of this technique, such as confocal microscopy [10], [11] and Raman spectroscopy [12], [13], were explored. The highest boosted resolution can reach sub-hundred nanometers [11]. Without using STED and STORM instruments, biological samples, such as virus and subcellular structures can be revealed with fluorescent labels [14] and in label-free [15] conditions.

The characteristics of microsphere-based super-resolution imaging, including magnification factor and resolution, were intensively studied [16]–[20]. The microsphere's size effect and refractive index (n) ratio to the imaging environment are essential for optimizing the imaging condition [9], [16], [18], [20]. In general, a high-refractive index dielectric sphere (approaching 2 or above) is beneficial for enhancing the coupling efficiency of evanescent waves, meanwhile an immersion medium is required to adjust sphere/environment index ratio below 2 to facilitate virtual imaging; otherwise, the focus position will be inside the sphere. Liquid immersion conditions, including partial immersion, can improve the image quality and contrast compared with using an air medium [18], [21]. In addition, small microspheres ($D<10$ μm) can achieve a best resolution of approximately $\lambda/7$, whereas large spheres ($D>50$ μm) can only reach approximately $\lambda/4$ [18]. The magnifying property of microspheres surpasses lenses with hemispherical (n) or superspherical (n^2) geometries and determines the minimum pixel size that can be recorded as an image. The highest reported magnification factor is approximately 10 [22]. Although a comprehensive explanation of the microsphere-based super-resolution imaging mechanism is still under debate [23]–[26], researchers have been making progress through simulations and specialized experiments [27], [28]. One commonly agreed principle for achieving super-resolution imaging using a microsphere is due to near-field coupling (e.g., evanescent waves), which carries and transforms high-spatial frequency information into its far-field counterpart (e.g. as propagation waves). Therefore, the microsphere must be placed within the proximity of the sample to interact with the evanescent waves that only exist within a distance of approximately 100 nm. The best achievable image resolution will be reduced without a proper control of the sphere–sample distance [9], [16], [29] and other unknown factors [30].

On the other hand, the limited field of view (FOV) of an individual sphere is one of the bottlenecks in microsphere-assisted nanoscopy. The estimated virtual image FOV of a microsphere is roughly a quarter of its diameter [18]. Therefore, a surface scanning functionality is necessary for the development of this technology. Optical trapping [31], [32], chemically driven [33] (by catalytic propulsion), and mechanical probe [34] methods have been used to manipulate microspheres. The first method requires specialized optical configurations and components for lasers, which are not readily available in general laboratories. The third method uses a glass micropipette for translating the microsphere, which is fragile and not robust for long term use. An alternative method involves an elastomer thin film with embedded microspheres for imaging and isopropyl alcohol as the lubricant for translating the film [35]. The reported film patch was around 1×1 cm^2 in size, which is flexible and mechanically robust compared with other methods. However, the positioning accuracy was relatively low and the gap between the sphere and sample was uncontrollable. A fixture-based microsphere with embedded sheet [36], [37] or chip [38], [39] was then developed. However, the friction between the scanning sheet and sample becomes a significant issue if the interface is not lubricated [36]. A large area in contact will induce large friction during translational movement.

To determine a reliable and precise position for pursuing the best imaging resolution, researchers assembled the microsphere using an atomic force microscope (AFM) cantilever and operated the scanning probe with ultra-high manipulation accuracy through a close-loop control mechanism. The gap between the microsphere and sample was controlled within the evanescent decay region, and a fast and highly reproducible lateral positioning was achieved [29], [40]. Some studies comprehensively analyzed the influence of sphere diameter, sphere–sample distance, and illumination angle on image quality. Super-resolution images with large areas are formed by stitching a sequence of raster-scanned frames; such images achieved approximately 200 times the acquisition efficiency of a conventional AFM [29]. In a recent study, a metal frame holder with the nanometer-level precision of a piezo stage was used to fix the microsphere and remotely scan above the sample surface, in which the sphere–sample distance was controlled at an accuracy of 1 nm [41]. The subhundred nanometer features, such as the 23–31 nm separations of paired nanodots and 50–60 nm nanogrooves, are distinguishable.

In our previous study [42], we explored the real and virtual imaging modes of barium titanate glass (BTG) and investigated the relationship between magnification factors and the focus position. By analyzing the streamlines of Poynting vectors through finite difference time domain simulation, we observed multiple intersecting positions, which could be perceived as image locations. This inference was verified using Blu-ray disk samples. The findings imply that a range of planes that can produce a clear image for microspheres and the effective magnification factor depends on the actual
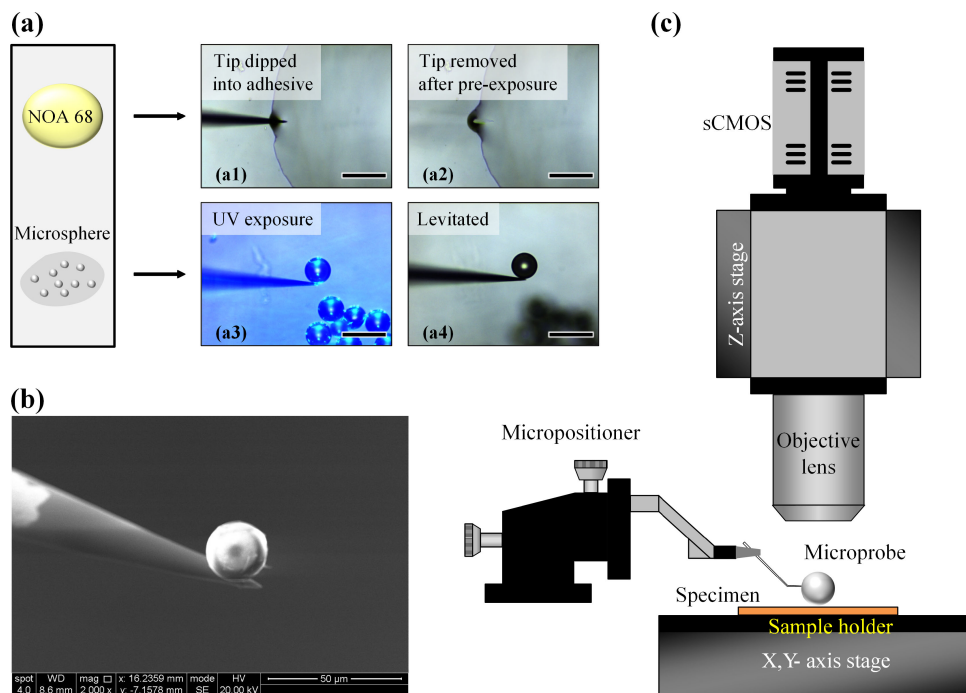
FIG. 1. Probe–lens device assembly for super-resolution imaging. (a) Assembly process of the probe–lens device. The dried BTG microsphere and a drop of NOA68 were prepared on a clean glass slide. The microprobe was dipped into the adhesive (a1), followed by a 2-s pre-exposure to UV, which left a trail in the adhesive after the removal (a2). After positioning the NOA-coated tip in contact with a selected microsphere (a3), a 90-s exposure was allowed to fully cure the NOA. Finally, the firmly bonded microsphere is levitated and moved around using the microprobe (a4); scale bar: 100 μm; (b) SEM image of the assembled 20-μm BTG microsphere on a tungsten microprobe with a tip diameter of 5 μm; (c) setup of the imaging system, which includes an Ni-E upright microscope platform equipped with Andor Zlya 5.5 sCOMS camera (5.5 megapixel), Intensilight mercury-fiber illuminator (C-LHGFIE), and nanoscale-resolution motorized stages in the X–Y (sample stage) and Z (focusing stage) axes. The micropositioner was fixed next to the sample stage to adjust the position of the microsphere relative to the objective lens and sample surface.

focus position. However, most studies focused on relatively simple or periodic sample patterns [9], [18], [42]; the image property analysis for arbitrary patterns is still lacking. Investigating the influence of focus position on magnification in accordance with the need for image consistency in performing large-area acquisitions over arbitrary feature samples is important. Therefore, an alternative versatile probe–lens scanning super-resolution imaging scheme is presented in this study. By placing the microsphere in contact with the sample using the probe and performing vertical scan of its imaging planes using the objective lens, we investigated the focusing characteristics of the arbitrary feature patterns and the correlation between the magnification factor and the actual focus plane. We also discussed the difference in the focusing characteristics of the microsphere virtual images of arbitrary and periodic patterns. The proposed method provides a quantitative way for determining the best focused plane and magnification that corresponds to the best achievable resolution. The finding presents some practical applications in large-area scanning microsphere nanoscopy.

II. FLEXIBLE ASSEMBLY OF THE PROBE–LENS DEVICE AND EXPERIMENTAL SETUP

The probe–lens device consists of a tungsten microprobe with an angle of 135° (PL-T5, Perfect LAB) and tip diameter of 5

μm and a BTG microsphere (Cospheric) with diameters of 5–20 and 60 μm and refractive index of 1.9. The device was inserted to a holder arm and manipulated on a 3D adjustable micropositioner (PT300, Perfect LAB). Fig. 1(a) illustrates the assembly process. A drop of microsphere solution was dispensed on a clean glass slide and either dried at the ambient humidity or on a hotplate. A drop of ultraviolet curable optical adhesive (Norland optical adhesive [NOA] 68, Norland) was dispensed near the microsphere region as the bonding material. The volumes of the microsphere solution and adhesive can be as small as 1–5 μL, which can be conveniently handled using a pipette. The microprobe tip was then dipped into the adhesive, followed by an approximately 2-s pre-exposure to UV light to coat a portion of the adhesive material in the tip surface (subset a1). The resulting trail (subset a2) shows the partially cured NOA, which is still elastic. Subsequently, the NOA-coated microprobe was manipulated to touch one of the microspheres, followed by a 90-s post-exposure to UV (subset a3). The firmly bonded microsphere was levitated and moved around using the tip (subset a4). An OmniCure S2000 UV light source was used to provide a power density of 50 mW/cm^2 for the pre- and post-exposure. According to NOA68 specification, a full cure requires an intensity of 4.5 J/cm^2. However, because the probe tip holds a minimal amount of adhesive, a 90-s exposure is sufficient based
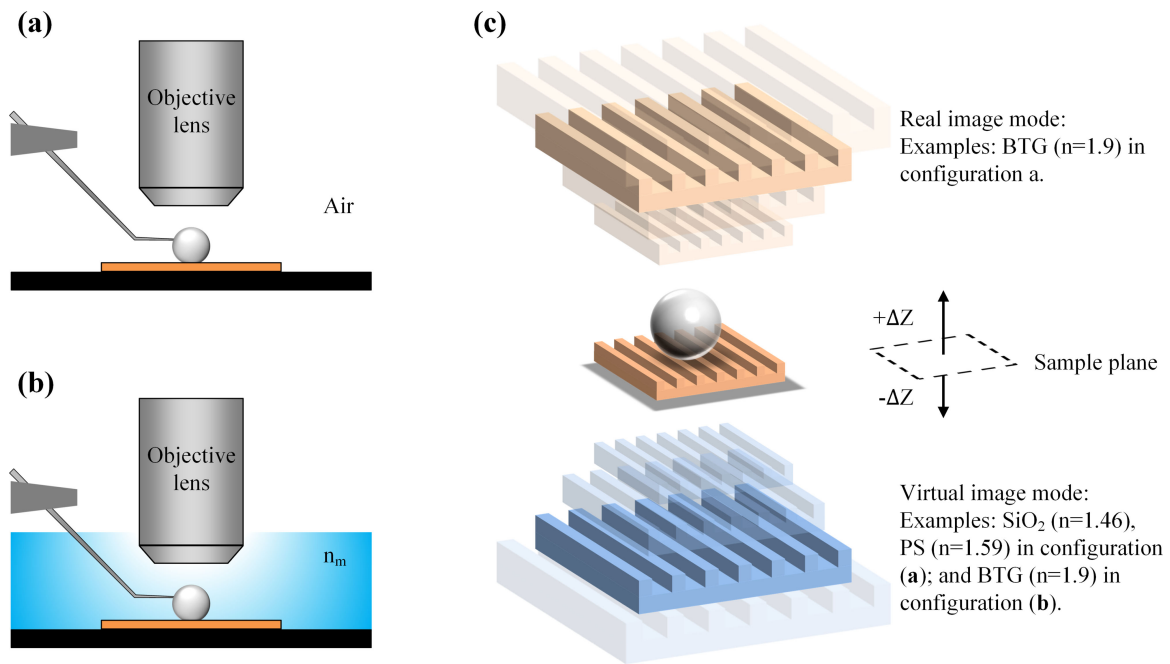
FIG. 2. Configurations of the imaging system. (a) Dry condition (air) imaging. The tip part (at least 13 mm, which is close to the radius of an 100x/0.90 objective lens) was bended 45° upwards to operate under the objective lens; (b) Liquid-immersed condition imaging; c available imaging modes. Real imaging applies when using high-index microspheres in an air medium, whereas virtual imaging applies when using high-index microsphere under liquid immersion or relatively low-index microspheres in air medium (e.g., SiO2 and PS).

on our experience [43]. The scanning electron microscope (SEM) photograph of an assembled BTG microsphere on a tungsten probe with a diameter of 20 μm diameter is shown in Fig. 1(b).

An upright optical microscope (Nikon Eclipse [Ni-E]) with coaxial illumination (reflection mode) and motorized sample and focusing stages was used for the observations (Fig. 1(c)). The stages and illumination were controlled using a personal computer with NIS-Elements Advanced Research software (Nikon). The light source (C-LHGFIE) provided white light illumination through a long-pass filter with a cutoff wavelength of 425 nm. The micropositioner was mounted on an external stage adjacent to the sample stage, and the probe–lens was placed on top of the sample surface as a secondary lens. The alignment of the microsphere with the main objective lens was set by manually adjusting the X, Y, and Z axes of the micropositioner. To minimize the gap between the microsphere and the sample surface, the probe position was slightly lowered after the former contacted with the latter. Owing to a certain degree of flexibility of the probe–lens device, a slight pressure was maintained on the surface throughout the experiment. The probe was fixed at an angle of 45° with respect to the axial direction of the holder arm. Therefore, a 135° angled probe is required to fit the tip part underneath the low-working distance (WD) objective lens and set it perpendicular to the sample surface. The length of the bended tip part should be no less than the radius of the objective lens used (e.g., 100×/NA 0.90 lens, WD = 1 mm, radius = 12 mm). A straight probe

can also be used when working under long-WD objective lens (e.g., 10 mm).

As shown in Figs. 2(a), (b), the probe–lens device can flexibly adapt to air- and liquid-immersed imaging configurations, respectively. Fig. 2(c) illustrates the possible imaging modes in the scheme. When using a microsphere with a relatively high index in an air medium, such as BTG (n = 1.9) [42], the super-resolution image is in real mode. By contrast, low-index microspheres, such as silica (SiO2, n = 1.46) [9] or polystyrene (PS, n = 1.6) [15], [18], [28], are in virtual imaging mode. Another virtual mode configuration is by immersing high-index microspheres in liquid, which can enhance the overall image quality and contrast [19]. Microspheres provide magnified images in multiple planes. In real image mode, the magnified image planes are located above the sample plane (e.g., surface), whereas the virtual ones are located below. The best focused plane and magnification factor must be determined to achieve high image quality with optimal resolution. In this study, we performed Z-axis scanning (Z-scan) over the feature patterns of the integrated circuits (ICs) from a central processing unit (CPU) sample.

III. RESULTS AND DISCUSSION

A. DETERMINATION OF THE MAGNIFICATION FACTOR AND PLANE OF FOCUS

In the experiments, four locations on the CPU sample with different patterns ([A], [B], [C], and [D]) were examined via Z-scan using water-immersed BTG microspheres with
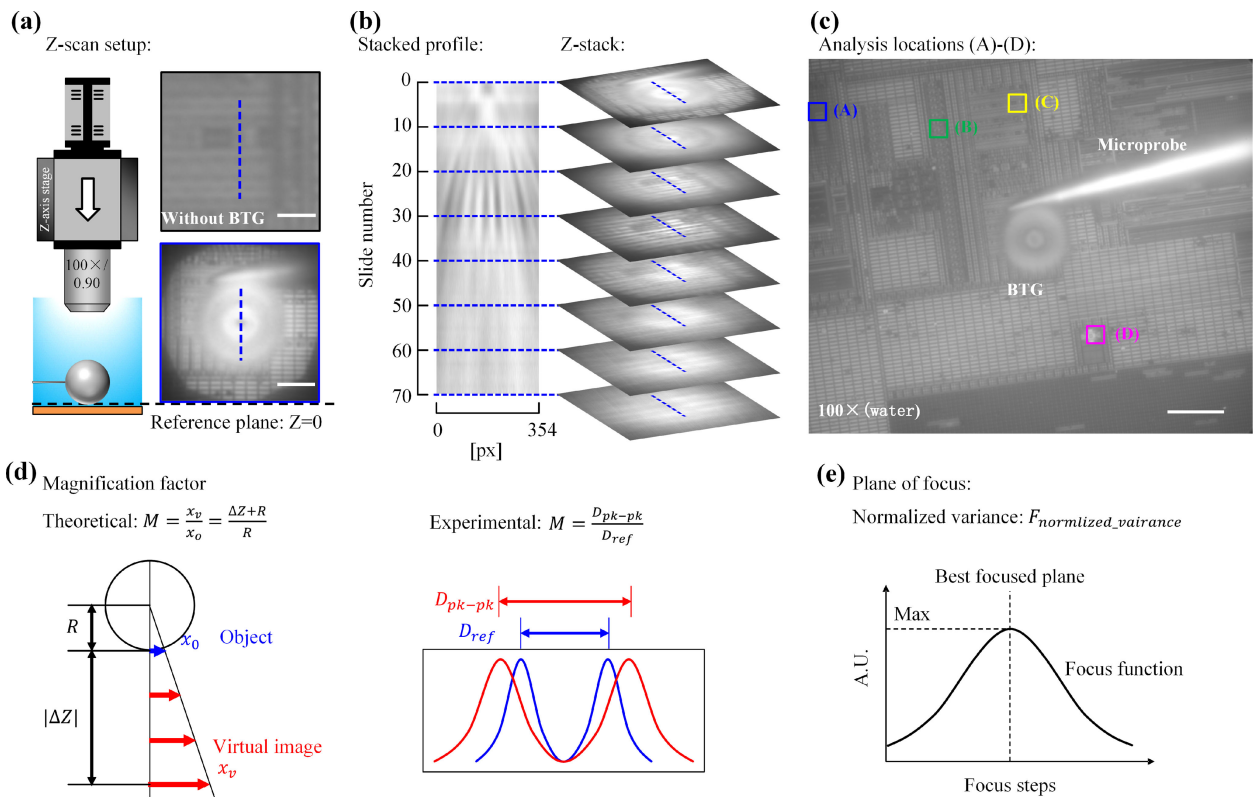
FIG. 3. Image acquisition for Z-scan experiment and analysis. (a) Z-scan setup. A sequence of images was taken under water-immersed condition with a Z-axis step size of 1 μm. The sample's focal plane (Z = 0) was set as the reference plane. The top subset image corresponds to the ICs pattern of a CPU sample imaged without BTG (100×/NA 0.90), whereas the bottom one shows the area with a BTG-attached probe on the CPU surface. A cutline (dashed blue line) with a length close to the sphere diameter in the 100× image scale across the microsphere was used for stack analysis. The diameter of the BTG in the plane of the first frame (Z = 0) was 21 μm; (b) Stacked profile showing the reconstructed cutline with respect to the slide numbers and its length in pixels. The length is adjusted depending on the actual feature pattern within the FOV. The corresponding Z-images at the selected planes are shown in the right; (c) 100× optical image of the IC, including locations (A), (B), (C), and (D) under Z-stack inspection; scale bar: 2 (top subset image in (a)), 10 (bottom subset image in (a)), and 20 μm; ((c)); (d) Theoretical estimation of the virtual image magnification of a spherical lens and the experimental determination based on the feature profiles; (e) Plane of focus determined through a focus function (normalized variance); the highest arbitrary unit score is used as the best focused plane.

diameters of 21 and 62 μm. The setup of the Z-scan experiments is shown in Fig. 3. A 100×/NA 0.90 objective lens was dipped into the water (n_m = 1.33) for imaging a decapsulated CPU sample (22 nm lithography, Intel G2010). When manually lowering the probe toward the sample, Newton's rings (e.g., diffraction) radiate from the center of the microsphere, which indicate contact with the surface (subset image of Fig. 3(a)). The probe position was fixed, and images were captured in series of Z-positions with a step of 1 μm. For each location, 70 and above 100 steps were recorded for the microspheres after a quick inspection of the imaging planes using the 21-μm and 62-μm BTGs, respectively. By extracting a line of interest (i.e., across the body of the microsphere) and reconstructing a stacked profile in the order of the slide numbers, a vertical view of the imaged structures was obtained. Subsequently, the slide numbers were calibrated based on the recorded height of the reference plane to obtain the relative Z-positions. Fig. 3(b) shows an example of the dataset of location (A) using the 21-μm BTG. Clear features are observed roughly between #20 and #35, thereby indicating a limited range of imaging planes.

Assuming that the distance between the bottom of the sphere and the object is zero as illustrated in Fig. 3(d), the theoretical estimation of the magnification factor based on geometrical optics can be expressed as

$$M = \frac{x_v}{x_o} = \frac{\Delta Z + R}{R}, \tag{1}$$

where x_o and x_v are the feature sizes of the object and its virtual image, respectively, R is the radius of the microsphere, and $|\Delta Z|$ is the relative distance between the virtual image and reference planes measured in the experiment. The experimental estimation is based on line profile analysis (Fig. 3(d)), in which the magnification factor was determined through the direct comparison of the feature size in the pixels with that in the reference image (e.g., conventional microscope image or an SEM image).

Normalized variance algorithm [44], [45] was used to evaluate the focus quality of each Z-stack image to assess its robustness to noise and overall performance [46]. This algorithm computes the variations in the intensity (gray scale) levels among image pixels and then uses a power function to
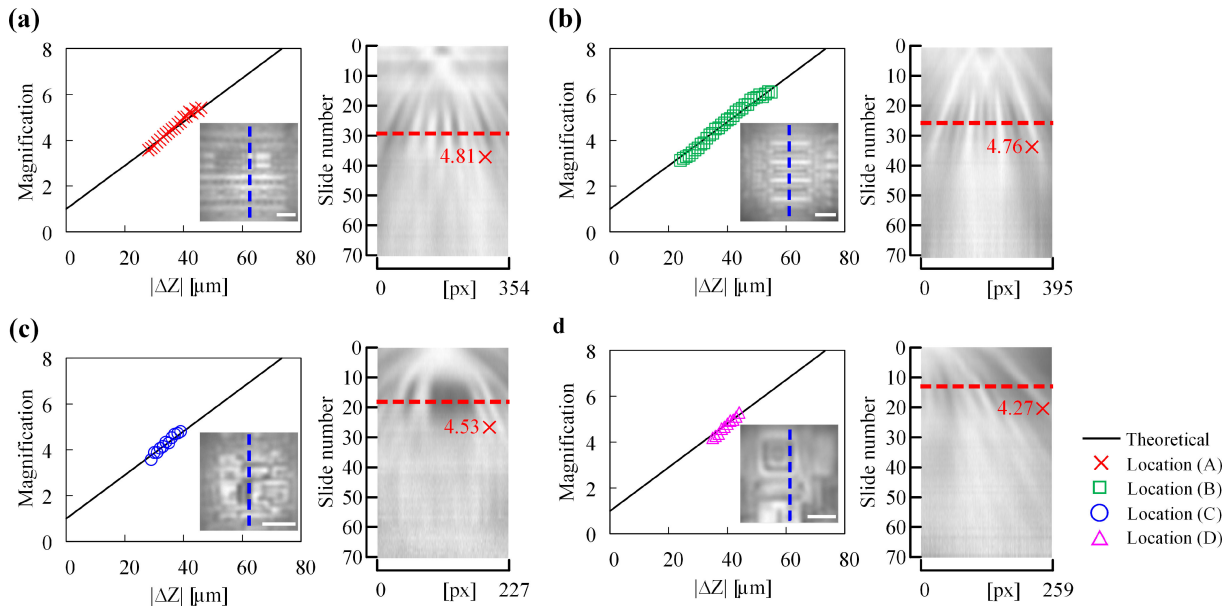
FIG. 4. Comparison of the Z-profiles of the different patterns. (a)–(d) The measured magnification factors were plotted against the corresponding theoretical values to analyze the patterns of locations (A), (B), (C), and (D). The inset images were cropped from the effective FOV of the calculated best focused position; scale bar: 1 μm. The BTG in this experiment (diameter = 21 μm) was used under a 100×/NA0.90 objective lens. The reconstructed stacked profiles are shown in the right; the width is in [pixel] and the length is represented by the slide numbers (the step between each slide is 1 μm in the Z direction). Location (B) has the most periodic pattern among the four, and its measurable data covered the longest range of magnification factor and |ΔZ|.

amplify the large differences from the mean intensity (μ).

$$F_{vairance} = \frac{1}{M \times N} \sum_M \sum_N \left[I_{(x,y)} - \mu\right]^2 \quad (2)$$

where I is the pixel intensity at pixel (x,y) and M and N are the height and width of the image, respectively. Then, the differences in the average image intensities among different images are compensated by normalizing the output using the mean intensity.

$$F_{normlized\_vairance} = \frac{1}{M \times N \times \mu} \sum_M \sum_N \left[I_{(x,y)} - \mu\right]^2 \quad (3)$$

As illustrated in Fig. 3(e), the best focused plane can be determined through the maximum score of the focus function, which is equal to 1 after normalization.

Fig. 4 shows the result of the 21-μm BTG experiments. The feature shape, width, and separation of each pattern are different. The measured and theoretical values of the magnification factor is plotted against |ΔZ| after calibration by normalizing the reference Z-positions to Z = 0. The results revealed that the measurable range of data of the patterns also exhibits variations. (B) shows the widest range of focus for a recognizable feature pattern among the four, whereas (C) and (D) have relatively narrow ranges. A similar trend is observed in the 62-μm BTG experiments. The pattern across the cut line is more periodic in (B) than in other patterns (shown in the insets). The stacked profiles are expressed in the slide numbers and pixels, and the best focused plane (slide) are indicated in red dashed lines with the corresponding magnification factor.

Fig. 5(a) shows the stacked plot of the magnification factors of the two BTG experiments. The consistency between the experimental measurement and theoretical prediction was evaluated using the R^2 values; $R^2 = 1 - \frac{RSS}{TSS}$, where RSS is the residual sum of squares and TSS is the total sum of squares (inset of Fig. 5(a)). The R^2 values of the 21-and 62-μm BTG experiments exceed 0.9 and 0.8, respectively. As shown in Fig. 5(b), the best focused BTG images revealed more details of the feature patterns compared with the bare objective lens images (100×/NA 0.90 dipped in water). The effective FOVs were determined using the size (e.g., diameter) of the center region of the microsphere without apparent spherical aberration. The FOVs of the 21- and 62-μm BTGs are approximately 4 and 9 μm, respectively.

The findings also indicate that the calibrated best focused plane of each experiment is consistent among BTG experiments with equal size. As shown in Fig. 6(a), the average best focused planes (|ΔZ|) for the 21- and 62-μm BTGs are at 38 and 87 μm, respectively. The table in Fig. 6(b) lists the estimated pixel sizes and magnification factors for the Z-scan experiments. The focus functions, which denote the focus characteristics of each pattern in the experiment, are plotted in Figs. 6(c)–Figs. 6(j). The best focused planes are represented by the slides that have the maximum value (i.e., 1).

B. RESOLUTION CHARACTERIZATION
Among the four locations, the smallest feature detected by the BTGs, which has a width of 50 nm, is found at (C). A thorough comparison of various scenarios was performed
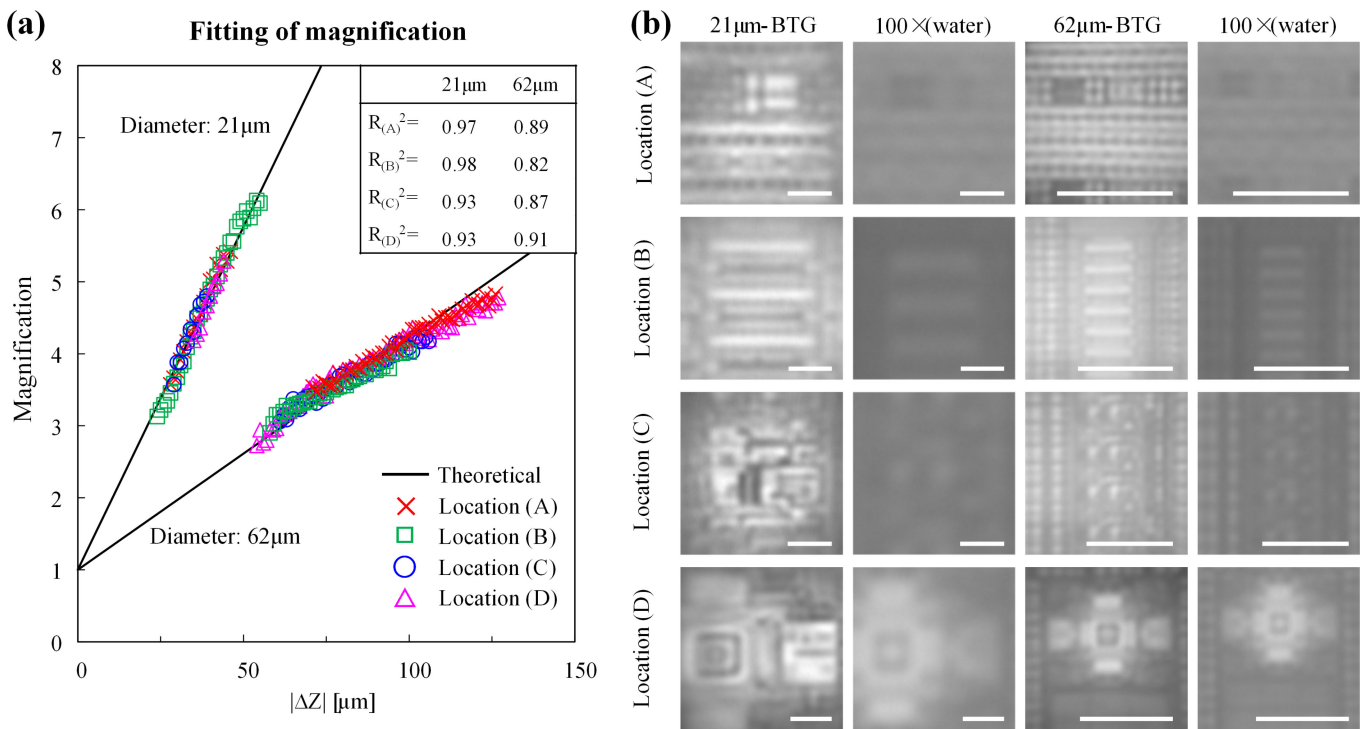
FIG. 5. Results of the magnification factors of the different patterns. (a) Measured and theoretical magnification factors obtained using the water-immersed 21- and 62-μm BTG microspheres. The data from locations (A), (B), (C), and (D) were collected and fitted with the theoretical result. The $R2$ of each dataset was calculated and presented in the inset; (b) Best focused BTG images of each pattern and the corresponding conventional microscope images taken using 100×/NA 0.90 objective lens dipped in water; scale bar: 1 μm for the 21-μm BTG and its 100× comparison group and 5 μm for the 62-μm BTG and its 100× comparison group.

(Fig. 7). The two yellow arrows in Fig. 7 indicate the two features that can only be resolved under the conditions shown in Figs. 7(c), (e). By conducting line profile analysis on the red dashed lines, we discovered that the resolution of the 21-μm BTG image is superior to those of larger BTG and conventional microscope images. Subsequently, the resolutions of each image were characterized by fitting them with Gaussian functions that have different values of full width at half maximum (FWHM). The fitted widths for the SEM and 21-μm BTG images are 50 and 130 nm, respectively.

C. LARGE AREA SUPER-RESOLUTION IMAGING

The probe–lens device can also be used for large-area acquisition by fixing the position of the sphere while scanning using the X–Y axes motorized stage. Figs. 8(a), (b) illustrate the imaging configuration and reconstruction processes, respectively. The microsphere was slightly pressed against the surface using the probe to maintain contact with the surface. No significant friction-induced dislocation of microsphere is observed during the experiment. The spacing for each step was set based on the effective FOV and focus plane of the microsphere. The recorded frames were cropped into smaller patches after acquisition. A high-resolution meta-image of the scanned area is obtained by stitching the patches according to the scan path and fusing them with 10%–20% overlapping area.

Fig. 9 shows a 20-by-5 scanned result of the 21-μm BTG under water immersion. The overall area is approximately 80 μm × 20 μm (1600 μm^2), and the meta-image is stitched using 100 patches with a size of 413 × 413 pixel. Figs. 9(a), (b) are the same area taken using the 100×/NA 0.90 objective lens in air and water media, respectively. The enlarged images (Figs. 9(d)–Figs. 9(l)) correspond to the previously examined locations ((A), (B), and (C)), which confirm a comparable super-resolution as observed in the Z-stack analysis. The SEM images of these patterns are taken as reference in Fig. 9(m)–Figs. 9(o). The estimated magnification factor for each frame is approximately 5.24–6.72×; the scanning time used is approximately 1 min. The meta-image in Fig. 9(c) shows more feature details than those in Figs. 9(a), (b).

D. INTERPRETATION OF MICROSPHERE MAGNIFICATION FACTORS

An interesting finding in our study is that when characterizing a microsphere superlens (for virtual image), using arbitrary and periodic feature patterns may result in different interpretations of the magnification factors. The findings of this work is complementary to our previous study [42], which only involved periodic pattern samples (e.g., Blu-ray disks). The virtual image projected by the microsphere at the far-field region has a broad intensity distribution in the Z-axis compared with a conventional microscope image. The intensity
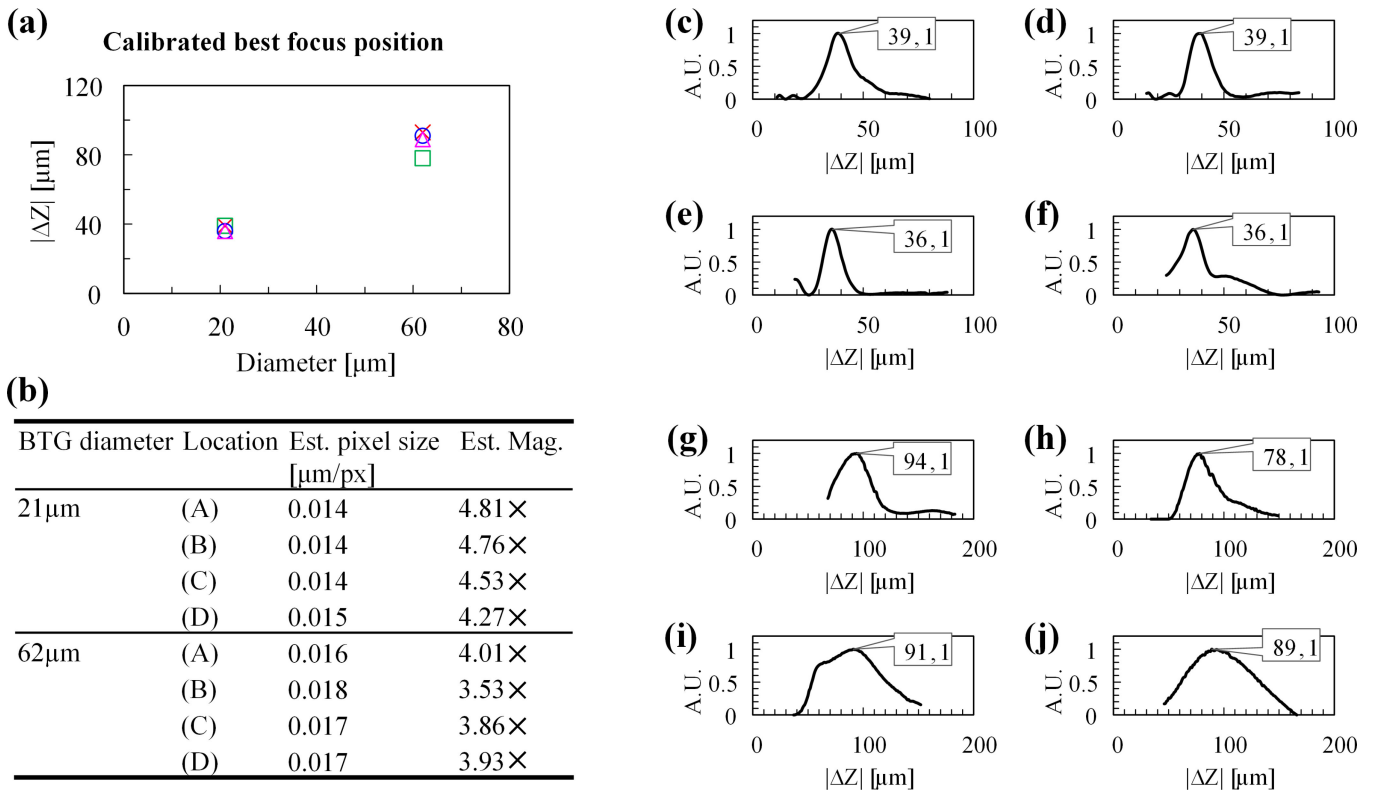
(b)

BTG diameter	Location	Est. pixel size [μm/px]	Est. Mag.
21μm	(A)	0.014	4.81×
	(B)	0.014	4.76×
	(C)	0.014	4.53×
	(D)	0.015	4.27×
62μm	(A)	0.016	4.01×
	(B)	0.018	3.53×
	(C)	0.017	3.86×
	(D)	0.017	3.93×

FIG. 6. Calibrated best focus position of the magnification factors. (a) Calibrated Z-position for each experiment using the best focused plane determined through the focus functions; (b) Summarized data of the pixel size and magnification factors for the 21- and 62-μm BTGs; (c)–(f) Focus functions plotted using recorded slides (slide #0 was selected near the plane with a clear image and not necessarily at Z = 0) for the 21-μm BTG at locations (A), (B), (C), and (D), respectively. An artificial unit was used for the value of the focus function, and the number of best focused slides with a maximum value of 1 was marked in each dataset; (g–j) Focus functions for the 62-μm BTG at the four locations, respectively.

distribution from other planes can be observed for a certain focus position, thereby creating an overlap of images with different magnification factors. This overlap is highly tolerant in imaging periodic patterns, such as the strips in a Blu-ray disk, because the "superpositioned" portion of the image is perpendicular to the stripe and therefore looks like the shrinking or broadening of the feature without a significant change in the main pattern. By contrast, the "superpositioned" portion of an arbitrary pattern can be observed in any directions in the plane and will easily accumulate to produce artifacts in the image and distort the main pattern. To define the best focused plane or the clearest microsphere super-resolution virtual image, a scenario with the maximum contrast between the pattern of interest and the background must be generated. One approach to create such scenario is developing a superlens with superior performance, such as the recently reported nanoparticle-based metalens [47], [48] that can produce a 45–50-nm white-light resolution. Another approach is through image processing, which can be performed using, but not limited to, statistical or derivative-based algorithms [46]. Derivative-based methods are highly sensitive to high-frequency images, which is beneficial for images with fine features, but possess low tolerance to noise. Conversely, statistical techniques (e.g., normalized variance algorithm) are robust to noise and produce

satisfactory accuracy. Therefore, we adopted the normalized variance algorithm to determine the best focused planes for the virtual images of BTGs. The third approach involves adjusting the illumination to enhance the signal-to-noise ratio. Wang [29] reported that the partial and inclined illuminations can improve image quality and range of the sphere–sample distance for acceptable imaging. This inference is supported by the experimental evidence the that middle illumination deteriorates image quality by increasing the propagating portion or background signals that overwhelms the high spatial frequency signals.

E. EXPLANATION ON ACHIEVED RESOLUTION
One of the most important advantage of microsphere-assisted super-resolution imaging is the ability of the sphere to produce high magnification factors. Previous studies achieved 6–8× magnification factors [9], [18], [42]. In this study, the magnification factors of the images at the best focused planes range within 4.27–4.81× for a 21-μm BTG, which can produce a pixel size of 0.015–0.014 μm/pixel; such size can theoretically resolve features as small as approximately 45 nm with 3 data points. The best characterized resolution obtained in this study is 130 nm, which is not among the reported highest achievable resolutions of microspheres in the past
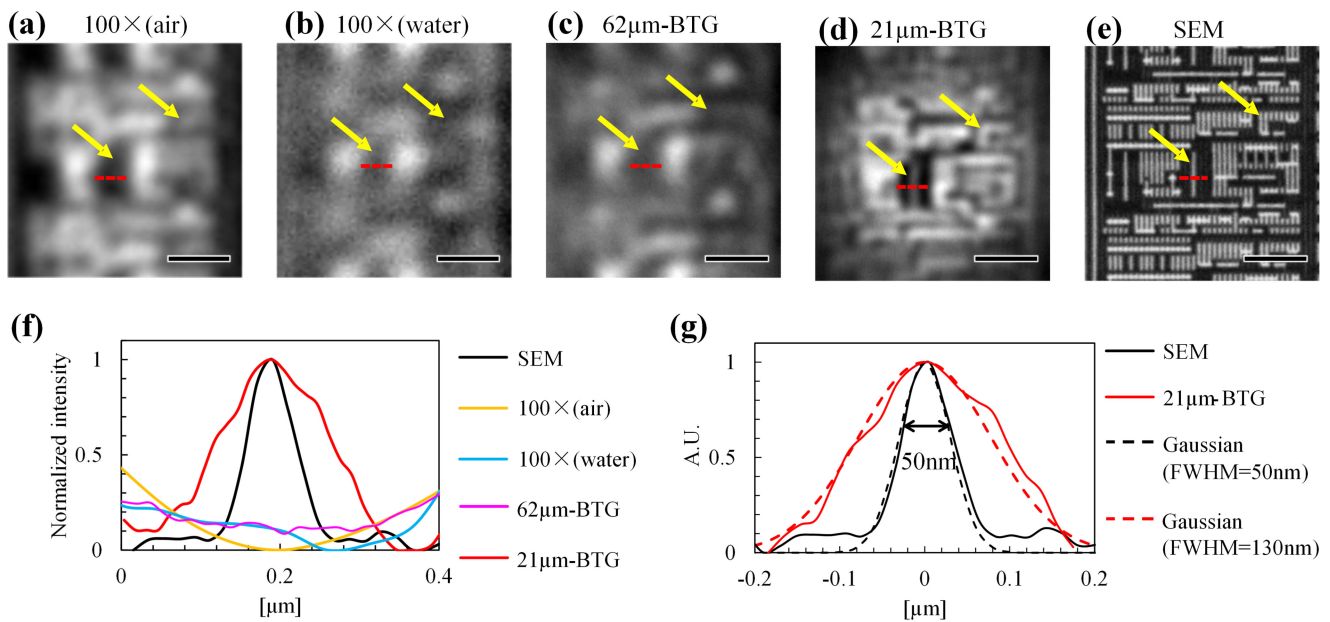
FIG. 7. Detected smallest features. (a) 100×-in-air; (b) 100×-in-water; (c) 21-μm BTG; (d) 62-μm BTG; (e) SEM images; scale bar: 2 μm. A 100×/NA 0.90 objective lens was used under water immersion condition for (a)–(d). The yellow arrows indicate that nanoscale features that are only resolvable in 21-μm BTG and SEM images. (f) Line profiles of the red dashed lines in (a)–(e)with normalized intensity. (g) Fitted result of a stripe feature resolved in the BTG and SEM images. After comparing with a Gaussian function with different FWHMs, the estimated profile shows that the length scale of the SEM and 21-μm BTG images are 50 (R2 = 0.94) and 130 nm (R2 = 0.96), respectively.
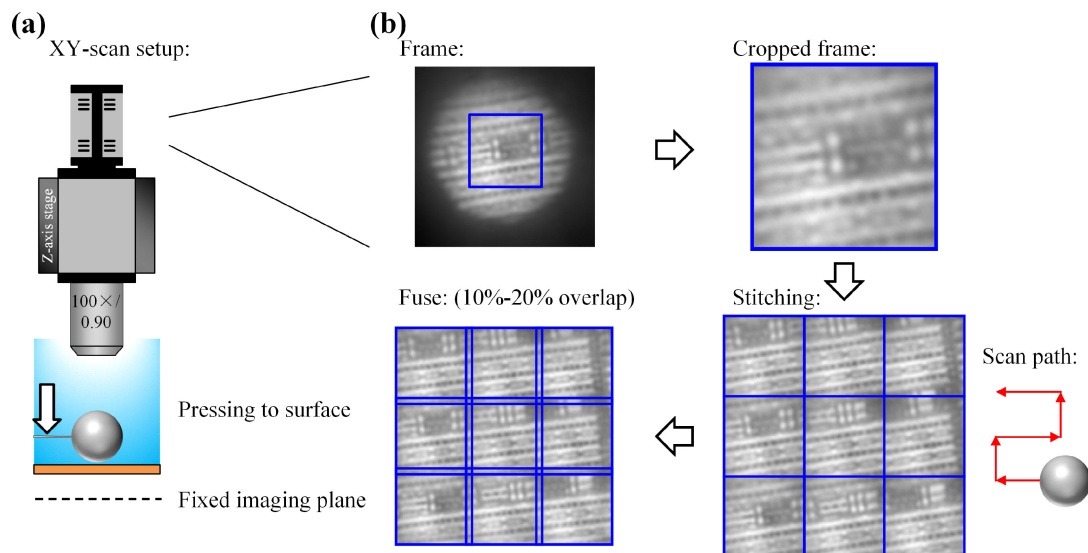

FIG. 8. Image acquisition for large-area scanning. (a) X–Y scan setup. The sample stage moves relative to the objective lens and microsphere in the X–Y plane in a zigzag path. The images were taken under water immersion condition. (b) Procedures of image processing and meta-image reconstruction. The obtained frames were cropped into small FOVs to avoid spherical aberration and stitched in accordance to the scan path. The final meta-image was fused with 10%–20% overlap. The ImageJ software (Fiji) was used for image processing and reconstruction.

decade. Many factors influence resolution characterization. First, the immersion medium and the objective lens are not optimized in this study. We used a standard objective lens for air imaging, which is not customized for liquid immersion imaging. As shown in Fig. 7, the quality of the images taken under 100×-in-water condition is inferior to that taken under 100×-in-air, and the quality of the 62-μm BTG image is

significantly higher than that of the 100×-in-water image but not superior to that of 100×-in-air image. For example, researchers achieved better results by using microspheres under oil immersion condition with optimized objective lens (i.e., 100×/NA 1.4) [41]. Second, the criteria used in previous studies for characterizing resolution are not unique. If the resolution is equal to the minimal feature size that can be discerned
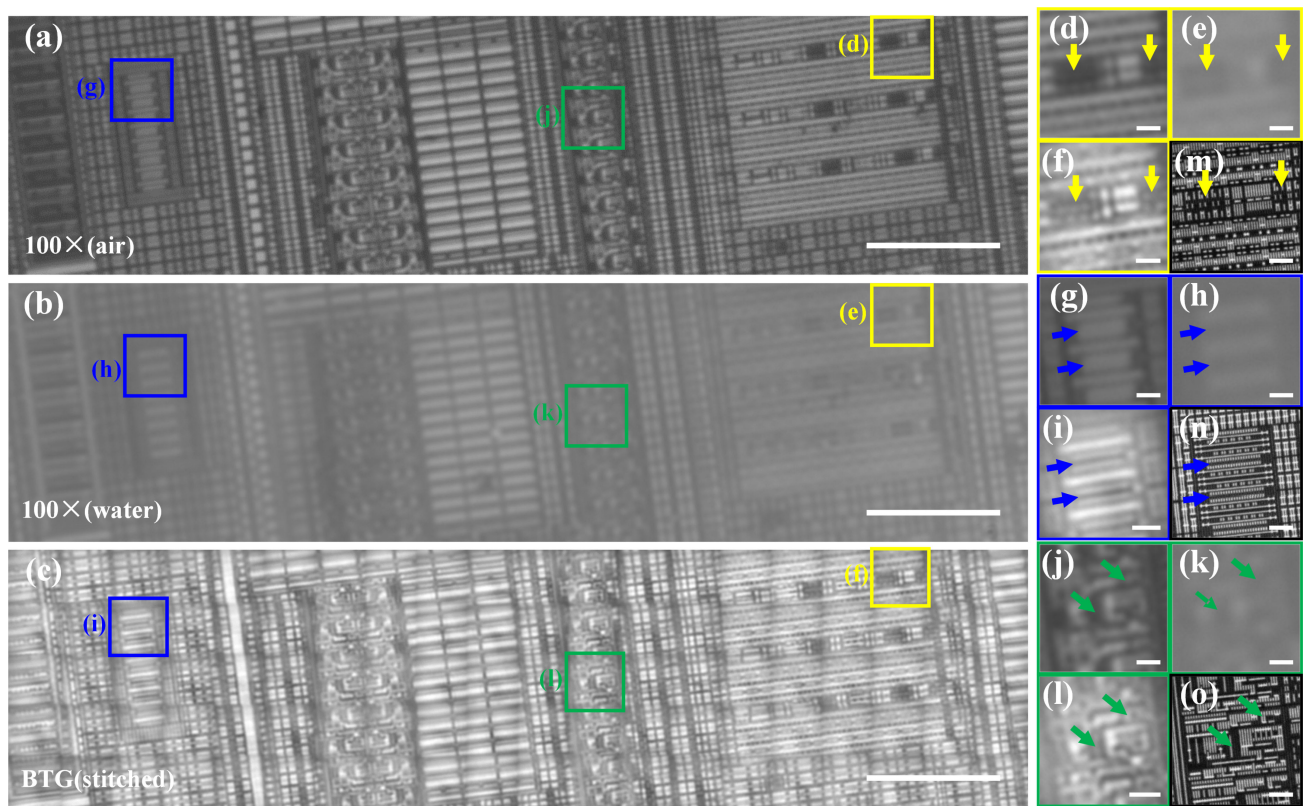
FIG. 9. Image acquisition for large-area scanning using the 21-μm BTG microsphere. Approximately 1600 μm2 area imaged using a 100×/NA 0.90 objective lens in (a) air and (b) water. (c) Reconstructed meta-image from a 20-by-5 BTG scan using a 21-μm BTG with a patch size of 413 × 413 pixel and overlap of 10%. The step size for Δx and Δy was 4 μm, and the scanning time was approximately 1 min. (d)–(l) Zoomed-in images labeled in (a)–(c). (m)–(o) SEM images (reference). Location (A): (d)–(f) and (m); Location (B): (g)–(i) and (n); Location (C): (j)–(l) and (o). The arrows in (d)–(o) indicate the nanoscale features that are only resolvable in BTG and SEM images. Scale bar: 10 μm for (a)–(c) and 1 μm for (d)–(o).

from the image, then the smallest feature in the present study can reach 50 nm. Although the sufficiently large separation from the adjacent features implies a clear observation, we only classify the observation for the 50-nm feature (Fig. 7) as detectable. A classical way to quantify image resolution is by fitting with PSF. This method is highly accurate and unlikely to overestimate the resolution values [35]. The comparison of the line profile with the Gaussian PSF with different widths indicated the best fit for the BTG image profile with an FWHM of 130 nm is the final resolution.

F. IMPROVEMENT AND PERSPECTIVES

The probe–lens assembly scheme offers the flexibility of using different kinds of microspheres that can be applied to real or virtual imaging modes. In real imaging, using high-index microsphere (e.g., BTG with n = 1.9) in air can support the integration of long-WD objectives with other components, such as robotic arms of adaptors with various functionalities. Virtual imaging can produce high resolution and image contrast and is feasible for scanning biological samples in liquid environments. To ensure the collection efficiency of evanescent waves from the surface, the probe is adjusted to steadily press the sphere against the surface. The flexibility of the probe can sustain minor bending without damaging the

assembly. We obtained a super-resolution meta-image with an area of 80 μm × 20 μm by scanning over a CPU sample using a 21-μm BTG. In addition, a 360 μm × 100 μm area was scanned using the 62-μm BTG. However, the latter exhibited many flaws in the reconstructed meta-image. For instance, the alignment accuracy for stitching is reduced due to the accumulated errors of the motorized stage and possible dislocation of the microsphere relative to the probe tip. This error is better tolerated in scanning small areas. Given an existing tilting of the surface, the consistent contact between the microsphere and the surface is not guaranteed as the scanning area increases. As a result, the image resolution deteriorates due to the induced gaps. Moreover, the focal plane is affected by the non-negligible slope of the surface, thereby producing inconsistent magnification factors for the frames that result in post-processing difficulties. Therefore, high-precision positioning equipment (e.g., piezo stages and a closed loop control system for the sphere position) must be installed. The current setup is sufficient for investigating the relationship between focal planes and magnification factors by examining arbitrary patterns (e.g., any specific locations).

Lastly, the correlation between image magnification factors and focal planes, which is determined using the acquired high-accuracy vertical data and automatic pattern recognition

software programs, is beneficial for detecting possible defects during scanning (e.g., dislocation) and improving the reconstruction quality. In addition, vertical data can be used to characterize resolutions and evaluate image quality improvement (e.g., partial and inclined illuminations) in 3D microsphere-assisted super-resolution imaging.

IV. CONCLUSION

In this study, we introduced a flexible and low-cost probe–lens device for scanning supper-resolution microscopy, which can readily accommodate versatile imaging configurations and can be applied to real or virtual imaging modes. By using water-immersed BTGs, we characterized the virtual image resolution and studied dependency of magnification factors on the focus positions. The observed correlation is consistent with theoretical predictions. For imaging arbitrary patterns, the ranges of measurable magnification factors for 21- and 62-μm BTGs are narrower than those for periodic patterns. We have demonstrated a universal method for quantitative measurement and definition of magnification factor and resolution of a microsphere virtual image for any feature pattern. The findings provide additional insights into the interpretation of arbitrary nanostructures through 3D optical imaging.

APPENDIX
A. IMAGE PROCESSING

Image processing and analysis were conducted using the ImageJ software (Fiji). The 100$\times$-in-air image (without microlens) with a calibrated pixel size of 0.065 μm/px was used as the reference image in determining the magnification factors of the BTG images. SEM images with pixel sizes of equal or less than 0.014 μm/px were used as reference images in analyzing the subdiffraction-limited features. The grid/collection stitch plugin in ImageJ was used for reconstructing the meta-images.

B. RESOLUTION CHARACTERIZATION

The Gaussian function is expressed as $G_{(x)} = e^{-\frac{1}{2}(\frac{x}{\sigma})^2}$, with variance of σ^2 which is calculated from $FWHM = 2\sqrt{2\ln(2)}\sigma$.

C. SCANNING ELECTRON MICROSCOPY CHARACTERIZATION

A field emission gun SEM (Model: Quanta 450 FEG-SEM, FEI) was used for the SEM imaging of the CPU sample. The beam voltage was 20 keV, with a spot size of 4.0 for high-resolution imaging.

ACKNOWLEDGMENT

REFERENCES

[1] A. Ernst, "Contributions to the theory of the microscope and the nature of microscopic vision," *Arch. Microscopic Anat.*, vol. 9, no. 1, pp. 413–418, 1873.

[2] Lord Rayleigh, "Investigations in optics, with special reference to the spectroscope," *Philos. Mag.*, vol. 8, no. 49, pp. 261–274, 1879.

[3] S. W. Hell and J. Wichmann, "Breaking the diffraction resolution limit by stimulated emission: Stimulated-emission-depletion fluorescence microscopy," *Opt. Lett.*, vol. 19, no. 11, pp. 780–782, 1994.

[4] M. J. Rust, M. Bates, and X. Zhuang, "Stochastic optical reconstruction microscopy (STORM) provides sub-diffraction-limit image resolution," *Nat. Methods*, vol. 3, no. 10, pp. 793–795, 2006.

[5] D. W. Pohl, W. Denk, and M. Lanz, "Optical stethoscopy: Image recording with resolution λ/20," *Appl. Phys. Lett.*, vol. 44, no. 7, pp. 651–653, 1984.

[6] B. Hecht *et al.*, "Scanning near-field optical microscopy with aperture probes: Fundamentals and applications," *J. Chem. Phys.*, vol. 112, no. 18, pp. 7761–7774, 2000.

[7] G. Binnig and H. Rohrer, "Scanning tunneling microscopy," *Helv. Phys. Acta*, vol. 55, no. 6, pp. 726–735, 1982.

[8] B. S. Luk'yanchuk, Y. W. Zheng, and Y. F. Lu, "Laser cleaning of solid surface: Optical resonance and near-field effects," *Proc. SPIE*, vol. 4065, pp. 576–587, 2000.

[9] Z. Wang *et al.*, "Optical virtual imaging at 50 nm lateral resolution with a white-light nanoscope," *Nature Commun.*, vol. 2, no. 1, 2011, Art. no. 218.

[10] A. Darafsheh, N. I. Limberopoulos, J. S. Derov, D. E. Walker Jr, and V. N. Astratov, "Advantages of microsphere-assisted super-resolution imaging technique over solid immersion lens and confocal microscopies," *Appl. Phys. Lett.*, vol. 104, 2014, Art. no. 061117.

[11] Y. Yan, L. Li, C. Feng, W. Guo, S. Lee, and M. Hong, "Microsphere-coupled scanning laser confocal nanoscope for sub-diffraction-limited imaging at 25 nm lateral resolution in the visible spectrum," *ACS Nano*, vol. 8, no. 2, pp. 1809–1816, 2014.

[12] P. K. Upputuri, Z. Wu, L. Gong, C. K. Ong, and H. Wang, "Super-resolution coherent anti-stokes Raman scattering microscopy with photonic nanojets," *Opt. Express*, vol. 22, no. 11, pp. 12890–12899, 2014.

[13] X. Zheng, C. Zong, M. Xu, X. Wang, and B. Ren, "Raman imaging from microscopy to nanoscopy, and to macroscopy," *Small*, vol. 11, pp. 3395–3406, 2015.

[14] H. Yang, N. Moullan, J. Auwerx, and M. A. M. Gijs, "Super-resolution biological microscopy using virtual imaging by a microsphere nanoscope," *Small*, vol. 10, no. 9, pp. 1712–1718, 2014.

[15] L. Li, W. Guo, Y. Yan, S. Lee, and T. Wang, "Label-free super-resolution imaging of adenoviruses by submerged microsphere optical nanoscopy," *Light Sci. Appl.*, vol. 2, 2013, Art. no. e104.

[16] X. Hao, C. Kuang, X. Liu, H. Zhang, and Y. Li, "Microsphere based microscope with optical super-resolution capability," *Appl. Phys. Lett.*, vol. 99, no. 20, 2011, Art. no. 203102.

[17] A. Darafsheh, "Optical super-resolution and periodical focusing effects by dielectric microspheres," Ph.D. dissertation, The Univ. North Carolina at Charlotte, 2013.

[18] A. Darafsheh, G. F. Walsh, L. Dal Negro, and V. N. Astratov, "Optical super-resolution by high-index liquid-immersed microspheres," *Appl. Phys. Lett.*, vol. 101, no. 14, 2012, Art. no. 141128.

[19] A. Darafsheh, "Influence of the background medium on imaging performance of microsphere-assisted super-resolution microscopy," *Opt. Lett.*, vol. 42, no. 4, 2017, Art. no. 735.

[20] S. Lee, L. Li, Z. Wang, W. Guo, Y. Yan, and T. Wang, "Immersed transparent microsphere magnifying sub-diffraction-limited objects," *Appl. Opt.*, vol. 52, no. 30, 2013, Art. no. 7265.

[21] S. Yang *et al.*, "Reduced distortion in high-index microsphere imaging by partial immersion," *Appl. Opt.*, vol. 57, no. 27, 2018, Art. no. 7818.

[22] P. K. Upputuri and M. Pramanik, "Microsphere-aided optical microscopy and its applications for super-resolution imaging," *Opt. Commun.*, vol. 404, pp. 32–41, 2017.

[23] A. V. Maslov and V. N. Astratov, "Optical nanoscopy with contact Mie-particles: Resolution analysis," *Appl. Phys. Lett.*, vol. 110, no. 26, 2017, Art. no. 261107.

[24] B. S. Luk'yanchuk, R. Paniagua-Domínguez, I. Minin, O. Minin, and Z. Wang, "Refractive index less than two: Photonic nanojets yesterday, today and tomorrow [Invited]," *Opt. Mater. Express*, vol. 7, no. 6, 2017, Art. no. 1820.

[25] L. Chen, Y. Zhou, Y. Li, and M. Hong, "Microsphere enhanced optical imaging and patterning: From physics to applications," *Appl. Phys. Rev.*, vol. 6, no. 2, 2019, Art. no. 021304.

[26] A. V. Maslov and V. N. Astratov, "Resolution and reciprocity in micro-spherical nanoscopy: Point-spread function versus photonic nanojets," *Phys. Rev. Appl.*, vol. 11, no. 6, 2019, Art. no. 064004.

[27] Y. Duan, G. Barbastathis, and B. Zhang, "Classical imaging theory of a microlens with super-resolution," *Opt. Lett.*, vol. 38, no. 16, 2013, Art. no. 2988.

[28] S. Lee, L. Li, Y. Ben-Aryeh, Z. Wang, and W. Guo, "Overcoming the diffraction limit induced by microsphere optical nanoscopy," *J. Opt.*, vol. 15, no. 12, 2013, Art. no. 125710.

[29] F. Wang *et al.*, "Scanning superlens microscopy for non-invasive large field-of-view visible light nanoscale imaging," *Nat. Commun.*, vol. 7, 2016, Art. no. 13748.

[30] R. Malureanu, O. Takayama, E. Shkondin, A. Novitsky, and A. V. Lavrinenko, "Microspherical nanoscopy: Is it a reliable technique?," *OSA Contin.*, vol. 3, no. 1, pp. 10–19, 2020.

[31] E. McLeod and C. B. Arnold, "Subwavelength direct-write nanopatterning using optically trapped microspheres," *Nat. Nanotechnol.*, vol. 3, no. 7, pp. 413–417, 2008.

[32] K. H. Leitz, U. Quentin, I. Alexeev, and M. Schmidt, "Process investigations of optical trap assisted direct-write microsphere near-field nanostructuring," *CIRP Ann. - Manuf. Technol.*, vol. 61, no. 1, pp. 207–210, 2012.

[33] J. Li *et al.*, "Swimming microrobot optical nanoscopy," *Nano Lett.*, vol. 16, no. 10, pp. 6604–6609, 2016.

[34] L. Krivitsky, J. J. Wang, Z. Wang, and B. Luk'yanchuk, "Locomotion of microspheres for super-resolution imaging," *Sci. Rep.*, vol. 3, 2013, Art. no. 3501.

[35] K. W. Allen *et al.*, "Super-resolution microscopy by movable thin-films with embedded microspheres: Resolution analysis," *Ann. Phys.*, vol. 527, no. 7–8, pp. 513–522, 2015.

[36] B. Yan *et al.*, "Superlensing microscope objective lens," *Appl. Opt.*, vol. 56, no. 11, 2017, Art. no. 3142.

[37] T. Zhang *et al.*, "Fabrication of flexible microlens arrays for parallel super-resolution imaging," *Appl. Surf. Sci.*, vol. 504, Oct. 2019, Art. no. 144375.

[38] G. Huszka, H. Yang, and M. A. M. Gijs, "Microsphere-based super-resolution scanning optical microscope," *Opt. Express*, vol. 25, no. 13, pp. 15079–15092, 2017.

[39] G. Huszka and M. A. M. Gijs, "Turning a normal microscope into a super-resolution instrument using a scanning microlens array," *Sci. Rep.*, vol. 8, no. 1, 2018, Art. no. 601.

[40] S. Wang, D. Zhang, H. Zhang, X. Han, and R. Xu, "Super-resolution optical microscopy based on scannable cantilever-combined microsphere," *Microsc. Res. Tech.*, vol. 78, no. 12, pp. 1128–1132, 2015.

[41] L.-W. Chen, Y. Zhou, M.-X. Wu, and M.-H. Hong, "Remote-mode microsphere nano-imaging: new boundaries for optical microscopes," *Opto-Electron. Adv.*, vol. 1, no. 1, 2018, Art. no. 17000107.

[42] H. S. S. Lai, F. Wang, Y. Li, B. Jia, L. Liu, and W. J. Li, "Super-resolution real imaging in microsphere-assisted microscopy," *PLoS One*, vol. 11, no. 10, 2016, Art. no. e0165194.

[43] B. Jia, H. S. S. Lai, F. Wang, L. Liu, G. Zhang, and W. J. Li, "Fabrication of a probe-lens device for scanning super-resolution imaging platform," in *Proc. of IEEE- 12th Int. Conf. Nano/Micro Engineered Mol. Syst.*, Los Angeles, CA, USA, 2017, pp. 327–332.

[44] F. C. A. Groen, I. T. Young, and G. Ligthart, "A comparison of different focus functions for use in autofocus algorithms," *Cytom. Part A*, vol. 6, pp. 81–91, 1985.

[45] T. T. E. Yeo, S. H. Ong, Jayasooriah, and R. Sinniah, "Autofocusing for tissue microscopy," *Image Vis. Comput.*, vol. 11, no. 10, pp. 629–639, 1993.

[46] Y. Sun, S. Duthaler, and B. J. Nelson, "Autofocusing in computer microscopy: Selecting the optimal focus algorithm," *Microsc. Res. Tech.*, vol. 65, no. 3, pp. 139–149, 2004.

[47] W. Fan, B. Yan, Z. Wang, and L. Wu, "Three-dimensional all-dielectric metamaterial solid immersion lens for subwavelength imaging at visible frequencies," *Sci. Adv.*, vol. 2, 2016, Art. no. e1600901.

[48] H. Zhu, M. Chen, S. Zhou, and L. Wu, "Synthesis of high refractive index and shape controllable colloidal polymer microspheres for super-resolution imaging," *Macromolecules*, vol. 50, no. 2, p. 660–665, 2017.

BOLIANG JIA received the B.S. degree in electronic engineering and the M.S. degree and biomedical engineering from The Chinese University of Hong Kong (CUHK), Hong Kong, in 2010 and 2011, respectively, and Ph.D. degree in mechanical engineering from the City University of Hong Kong (CityU), Hong Kong, in 2019. He is currently working as a Postdoctoral Fellow in the same department in City University investigating new materials and fabrication methods of optical superlens for super-resolution imaging.

PAN LI received the B.S. degree in mechanical engineering from Zhengzhou University in 2012, and Ph.D. degree in mechanical and electrical engineering from the University of Chinese Academy of Science (UCAS), Shenyang Institute of Automation (SIA), Chinese Academy of Science (CAS), China, in 2020. She is currently working as a Lecturer with the Department of Mechanical and Electrical Engineering, Hohai University, China, investigating dielectric micro-objects-based nano-optics and nanoengineering, including super-resolution optical imaging and nanopatterning.

FEIFEI WANG received the BE degree from the Agriculture University of Hebei, China, in 2011 and the Ph.D. degree in mechanical and electronic engineering from the Shenyang Institute of Automation (SIA), Chinese Academy of Sciences (CAS). He is currently working as a Postdoctoral Research Fellow in the chemistry department in Stanford University. His research interests include micro/nano fabrication, super-resolution imaging and near infrared II imaging.

HOYIN CHAN received the B.S. and M.S. degrees in mechanical and automation engineering from The Chinese University of Hong Kong, Hong Kong, and the Ph.D. degree from Michigan State University, USA. After returning to Hong Kong in 2008, he joined Hong Kong Applied Science and Technology Research Institute Company Limited (ASTRI) for four years and worked on numerous MEMS sensor and actuator projects including micro-flow sensors and micro-mirrors. Particularly, he worked on designing and manufacturing of a MEMS scanning mirror for pico-projection applications. In 2013, he joined the Department of Mechanical Engineering (formerly the Department of Mechanical and Biomedical Engineering), City University of Hong Kong as a Research Fellow. In 2019, he was promoted as a Research Assistant Professor. His research interests include micro/nano sensors and actuators, Lidar, artificial intelligence and biomedical devices.

GUANGLIE ZHANG received the BE and ME degrees in electronic engineering and the Ph.D. degree in control science and engineering from Xi'an Jiaotong University (XJTU), China, in 1997, 2000, and 2003, respectively. He is currently working as a Research Associate Professor with the Department of the Mechanical Engineering, City University of Hong Kong (CityU). His research interests cover areas of micro/nano biotechnology, human-motion recognition algorithms, and complex-sensor-network fusion algorithms.

WEN JUNG LI received the B.S. and M.S. degrees in aerospace engineering from the University of Southern California (USC), in 1987 and 1989, respectively, and the Ph.D. degree in aerospace engineering from the University of California at Los Angeles (UCLA), in 1997. From 1997 to 2011, he was with the Department of Mechanical and Automation Engineering, The Chinese University of Hong Kong. He was with Aerospace Corporation, El Segundo, CA, USA, the NASA Jet Propulsion Laboratory, Pasadena, CA, USA, and Silicon Microstructures, Inc., Fremont, CA, USA. He has served as the President of the IEEE Nanotechnology Council, in 2016 and 2017. He is currently a Chair Professor with the Department of Mechanical Engineering, City University of Hong Kong. His current research interests include intelligent cyber physical sensors, super-resolution microscopy, and nanoscale sensing and manipulation.